Pergamon

Cement and Concrete Research 31 (2001) 953–958

CEMENT AND CONCRETE RESEARCH

Chemical mapping of thaumasite formed in sulfate-attacked cement mortar using near-infrared Raman imaging microscopy

Karim N. Jallad[a,*], Manu Santhanam[b], Menashi D. Cohen[b,1], Dor Ben-Amotz[a]

[a]*Department of Chemistry, Purdue University, 1393 Brown Building, West Lafayette, IN 47907, USA*
[b]*School of Civil Engineering, Purdue University, West Lafayette, IN 47907, USA*

Received 3 January 2001; accepted 25 March 2001

Abstract

This work reports a new method for identifying and mapping the distributions of both thaumasite and ettringite in cement using near-infrared Raman imaging microscopy (NIRIM). This technique offers an important alternative to conventional X-ray diffraction (XRD) and scanning electron microscopy (SEM), which cannot easily distinguish preexisting ettringite from thaumasite formed as the result of sulfate attack. The NIRIM instrument used for these studies combines fiber-bundle image compression (FIC) hardware and multivariate signal processing software to identify and map chemical species in cement samples produced with and without extended exposure to sulfate. The NIRIM images clearly reveal thaumasite, ettringite, and gypsum microstructures. Cement paste formed in a carbon dioxide environment is found to contain both ettringite and gypsum species, while NIRIM images of cement exposed to sulfate reveals only thaumasite and gypsum. The NIRIM results are shown to correlate well with combined SEM/X-ray microanalysis of the same samples. © 2001 Elsevier Science Ltd. All rights reserved.

Keywords: SEM; Image analysis; Sulfate attack; Ettringite; Raman imaging

1. Introduction

Sulfate attack is a complicated phenomenon that involves both physical and chemical alterations to concrete. Reactions between sulfate ion-bearing water and cement hydration products result primarily in the formation of gypsum ($CaSO_4 \cdot 2H_2O$), ettringite ($6CaO \cdot Al_2O_3 \cdot 3SO_3 \cdot 32H_2O$), thaumasite ($CaCO_3 \cdot CaSO_4 \cdot CaSiO_3 \cdot 15H_2O$), and an alteration of the structure of the calcium silicate hydrate (C-S-H) gel [1,2]. Physically, the effect is manifested in the form of expansion, surface spalling and softening, and overall loss of cohesiveness of the concrete. Thaumasite is reported to form primarily at low temperatures (0–5°C) during sulfate attack, when there is an available source of CO_3^{-2} (which could either be limestone dust, which is being increasingly used as a filler, or limestone aggregate [2]). Thaumasite is stable till temperatures of about 15°C [2]. The thaumasite form of sulfate attack has been recognized to be particularly deleterious because its formation involves the C-S-H itself. The characteristic feature of thaumasite formation is to transform the surface of the concrete into a soft pulpy mass [3]. Traditional methods of protection against sulfate attack, such as the use of low C_3A cements, are not effective in this case. Recent studies have shown that low temperatures need not be necessary for thaumasite formation [4].

In this study, the spatial distribution of thaumasite in sulfate-attacked cement mortar is examined. Of the techniques that have been used to date to analyze cement systems containing thaumasite, few offer the ability to map the 2-D distribution of thaumasite in these cement systems. Scanning electron microscopy (SEM) with X-ray microanalysis can identify thaumasite from large down to trace amounts. However, ettringite and thaumasite have similar microstructural features in images obtained by SEM in the conventional high vacuum mode [5,6]. Thus, thaumasite identification in the SEM currently relies on X-ray microanalysis. Many analyses and a significant experience are needed to determine whether the material being examined is thaumasite, sulfate-rich C-S-H gel, or a mixture of C-S-H gel and gypsum or ettringite [7]. X-ray diffraction (XRD) can give a clear indication of the crystalline phases. How-

* Corresponding author. Tel.: +1-765-494-5591.
E-mail addresses: jallad@purdue.edu (K.N. Jallad), mcohen@ecn.pursue.edu (M.D. Cohen).
[1] Tel.: +1-765-494-5018; fax: +1-765-496-1364.

0008-8846/01/$ – see front matter © 2001 Elsevier Science Ltd. All rights reserved.
PII: S0008-8846(01)00514-2

ever, ettringite and thaumasite have similar crystal structures [8], thus their XRD patterns show similarities [9]. The spectroscopic techniques that are commonly used to gather chemical information, such as Raman spectroscopy, provide spatially averaged data and tell us little about the distribution of thaumasite across sulfate-attacked cement mortar surfaces. We present here resolved chemical maps of thaumasite on sulfate-attacked cement mortar surfaces using near-infrared Raman imaging microscopy (NIRIM).

2. Experimental

2.1. Materials

Samples of natural thaumasite (Patterson, NJ) were purchased from Ward's Natural Science. Reagent grade gypsum was used. Ettringite was prepared in the laboratory by mixing solutions of calcium oxide and aluminum sulfate in 1:6 molar ratio and filtering the resulting white precipitate in an air bag with a nitrogen gas purge [10]. The white precipitate was dried under nitrogen. The dried powder was confirmed to be ettringite by XRD. The mortar was prepared in accordance with ASTM C109 using an ASTM Type I Portland cement and ASTM C778 graded sand. Cylindrical specimens of 23 mm diameter $\times$ 80 mm height were prepared. The initial curing period was 14 days in saturated limewater, following which, the specimens were completely immersed in a sodium sulfate solution (equivalent $SO_3 \cong 25{,}000$ ppm) and stored in a controlled room temperature at $5 \pm 2^{\circ}C$. After 200 days of immersion in the solution, the specimens were removed. The cylindrical specimen was cut into a 1-cm thick piece using a saw, and was then dried for observation under the NIRIM; it was further embedded with epoxy for observations under SEM.

2.2. Chemical imaging

Raman images of the samples were collected using the NIRIM imaging technique shown schematically in Fig. 1 [11]. This instrument is based on the latest fiber-bundle image compression (FIC) design, a technique that allows the simultaneous collection of a complete spectral 3-D data cube in one read-out of a CCD detector [12,13]. In this FIC-based instrument, the light propagates from the sample to the spectrograph through an optical fiber bundle [14]. At the collection end, the optical fibers are ordered in a square array where each fiber collects light from a unique spatial point in the sample. At the distal end of the bundle, the optical fibers are ordered in a linear stack, which serves as the entrance of an imaging spectrograph. The FIC fiber bundle used in the NIRIM consists of eighty 50-μm core diameter fibers ordered in a 10×8 square array at the collection end (Fiberoptic Systems). The linear stack is attached to an imaging spectrograph (Kaiser Optical Systems, Holospec f/1.8) and provides 80 Raman spectra per

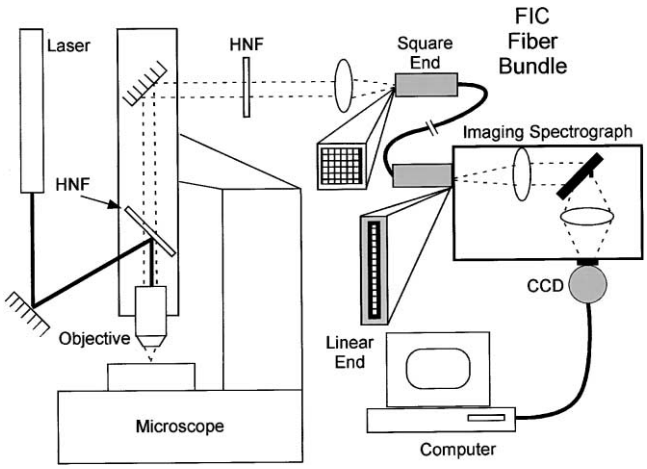

Fig. 1. Schematic diagram of the NIRIM showing the 785-nm diode laser, FIC fiber bundle, imaging microscope, and computer.

image frame, each with 900 wavelength channels (spanning a 75- to 1850-cm^{-1} Raman shift window with a spectral resolution of 2 cm^{-1}). The sample is imaged onto the fiber bundle by optically coupling the bundle to an Olympus BX-60 microscope. A $\times 20$ microscope objective (Olympus IC-20) yields a single-frame field of view of 70×56 μm with a spatial resolution of 7 μm per FIC image pixel. The sample is globally illuminated by a 500-mW diode laser (SDL-8630) operating at 785 nm with a total power of about 80 mW of the 785 nm reaching the sample field of view (or about 1 mW of excitation power per Raman spectrum). Besides the imaging capabilities of the NIRIM system, the system can be used as a conventional Raman microscope where a single-frame field of view will give one average spectrum (single-frame exposure) corresponding to the sum of all 80 Raman spectra in a single-image frame.

2.3. Data analysis

3-D data cubes acquired from the sulfate-attacked cement mortar sample were analyzed using the Multispec spectral image processing software package [15], which facilitates the creation of single- or multiple-channel chemical images using a variety of feature selection, training, and classification algorithms such as spectral angle mapping (SAM) classifiers. However, in order to enhance the performance of the Multispec program in classification, the data was preprocessed using Savitsky–Golay [16,17] second derivative (SGSD). The SGSD algorithm is used to efficiently filter out both pixel correlated noise and broad background interference while preserving the chemical information content of the Raman spectral features. The optimum Raman signal enhancement is obtained when the data are processed with a nine-point SGSD window width as shown in Fig. 2. In addition, the last 80 data points in the original spectra were truncated before SGSD preprocessing to eliminate artifacts close to the laser wavelength resulting from the holographic notch filter. After SGSD preprocessing, the

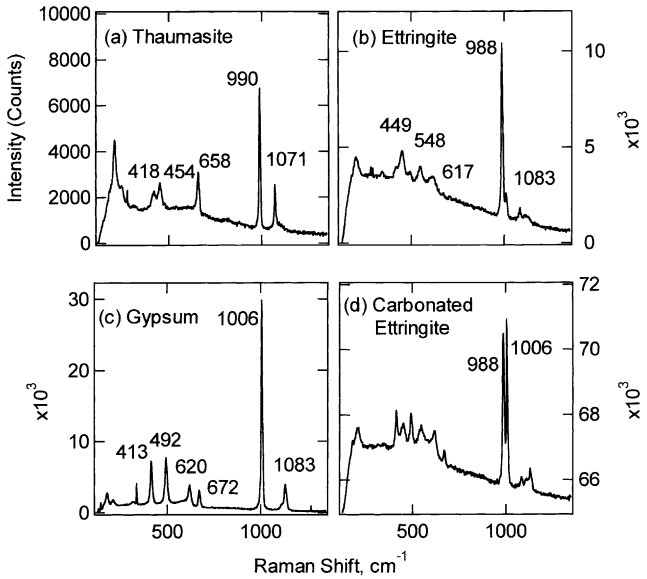

Fig. 2. Raman spectra of powdered cement components obtained using a single NIRIM image frame in 120 s of integration time, using a laser power of approximately 80 mW (with a ×20 objective, corresponding to a 70×56-μm^2 area).

chemical images were produced using the SAM classification algorithm. This was done by building a training library consisting of spectra belonging either to background, thaumasite, gypsum, or ettringite. The SAM algorithm then compared each individual image pixel to the different classes in the library, and assigned the pixel to the class it best resembles, as defined by the correlation between the image and library spectra. A correlation coefficient near 1.0 indicates a strong similarity between the spectra and the classes. In particular, we have set the correlation coefficient threshold to .85, thus making the algorithm very selective in assigning the spectra to the different classes. The assignment of an image pixel to a class is binary; either it belongs to the class or it does not. Consequently, the final processed chemical images of the solid surfaces classify the image into regions labeled according to the predominant chemical species in each region, but do not contain any quantitative intensity or concentration information.

3. Results and discussion

Single-frame exposure Raman spectra of thaumasite, ettringite, and gypsum, collected using the NIRIM, are shown in Fig. 3. Each spectrum was the result of 120 s integration. As seen in the first spectrum (Fig. 3(a)), Raman peaks corresponding to phonons from thaumasite at 418, 454, 658, 990 (strongest peak), and 1071 cm^{-1} are evident [18,19]. In the second spectrum (Fig. 3(b)), features are observed at 449, 548, 617, 988 (strongest peak), and 1083 cm^{-1}, which are assigned to ettringite. The spectrum illustrated in Fig. 3(c) shows intense features appearing at 413, 492, 620, 672, 1006 (strongest peak), and 1071 cm^{-1},

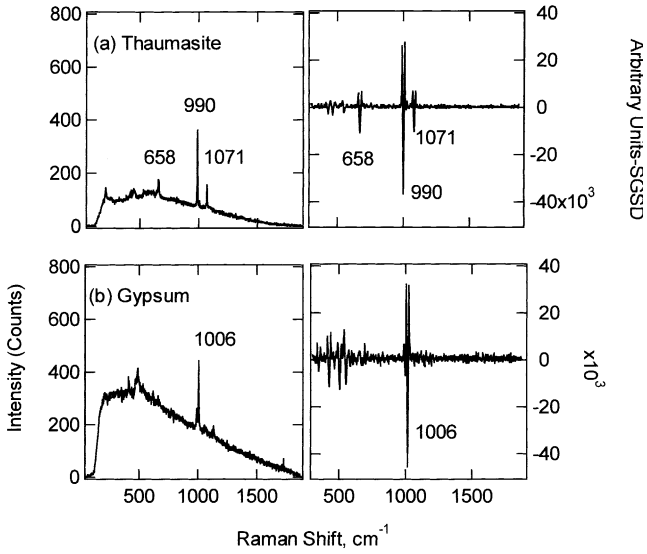

Fig. 3. The left frames contain Raman spectra and the right frames contain corresponding SGSD preprocessed Raman spectra.

which correspond to gypsum. In the case of thaumasite, the two Raman peaks at 658 and 1071 cm^{-1} will help in distinguishing thaumasite from either gypsum or ettringite. As shown in Fig. 3(d), the two strongest peaks of ettringite and gypsum are clearly resolved at 988 and 1006 cm^{-1}, respectively, showing the ability of the NIRIM to separate the two components if both are present in the sample.

Before taking a Raman image of the sulfate-attacked cement mortar, an image of thaumasite, ettringite, and gypsum microcrystals mixture was taken. The image shown in Fig. 4(a) is composed of 10×10 (100) frames corre-

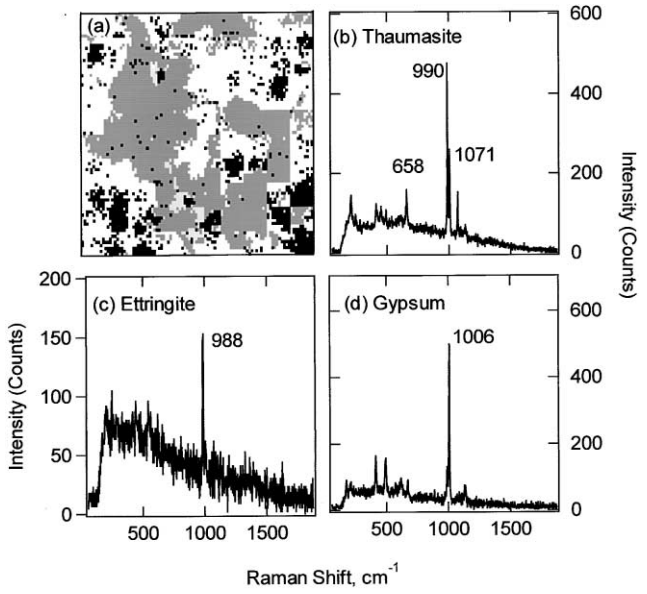

Fig. 4. (a) Chemical image of a 700×560-μm^2 region of the microcrystalline powder mixture. The grey areas correspond to ettringite, while the light and dark areas indicate gypsum and thaumasite, respectively. (b, c, d) Representative single fiber Raman spectra from the microcrystals mixture.

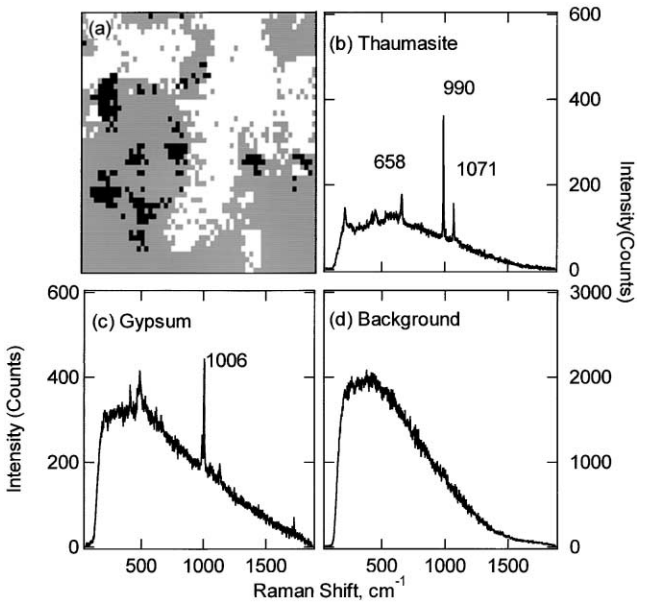

Fig. 5. (a) Chemical image of a 420×336-μm^2 region of the sulfate-attacked cement mortar surface. The grey areas correspond to background, while the light and dark areas are assigned to gypsum and thaumasite, respectively. (b, c, d) Representative Raman spectra from the sulfate-attacked cement mortar surface.

sponding to 700×560 μm^2 area of the microcrystalline solids mixture. The total exposure time was 5 1/2 h (200 s/frame) using the $\times 20$ objective that corresponds to a single fiber resolution of 7×7 μm^2 area. Using the SAM classification algorithm and without SGSD data preprocessing (no broad background interference), each pixel of the 8000 (100×80) pixels in the entire Raman image is

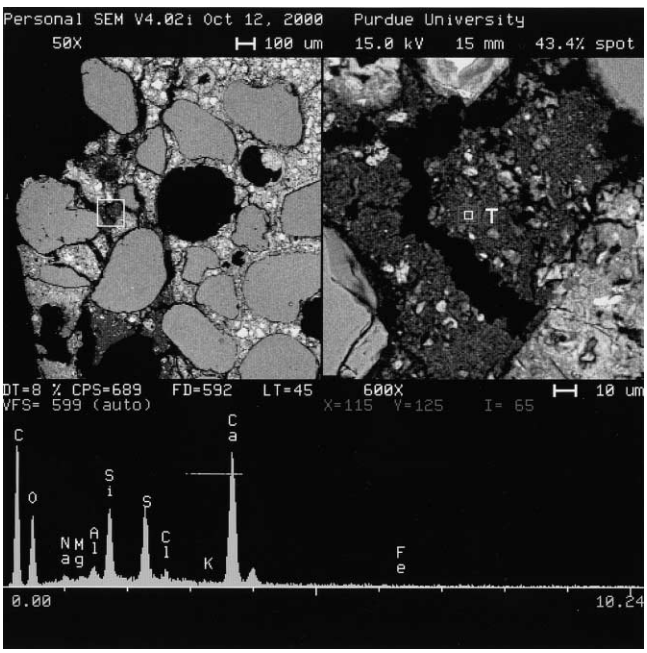

Fig. 6. SEM image of abundant thaumasite formation (represented by the dark area) near the surface of the cement mortar.

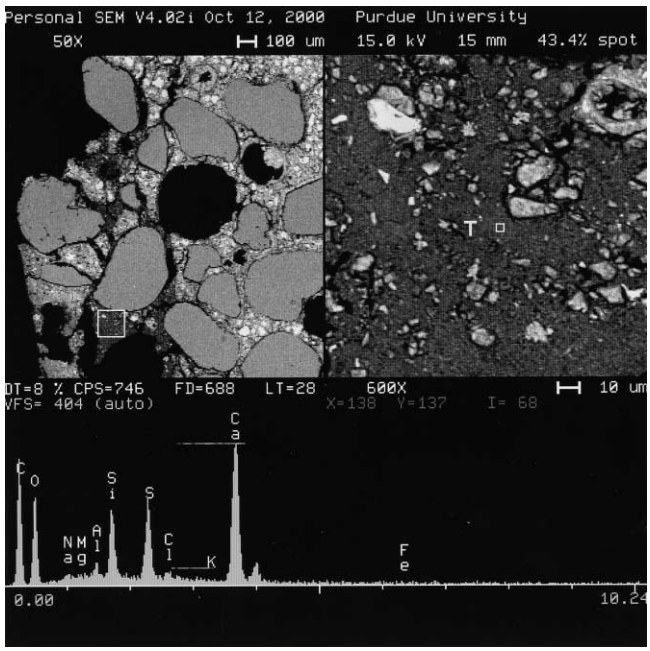

Fig. 7. SEM image of a large area where C-S-H has been completely transformed to thaumasite, which is seen as the dark deposit on the right-hand side image.

categorized as thaumasite, ettringite, or gypsum based on the Raman spectrum associated with that pixel. The spectrum obtained at each of the 8000 (100×80) pixels of the Raman image (Fig. 4(a)) falls into one of three distinct categories. Fig. 4(b–d) illustrate representative examples of three types of Raman spectra obtained from the microcrystalline solids mixture. The first spectrum (Fig. 4(b)) repre-

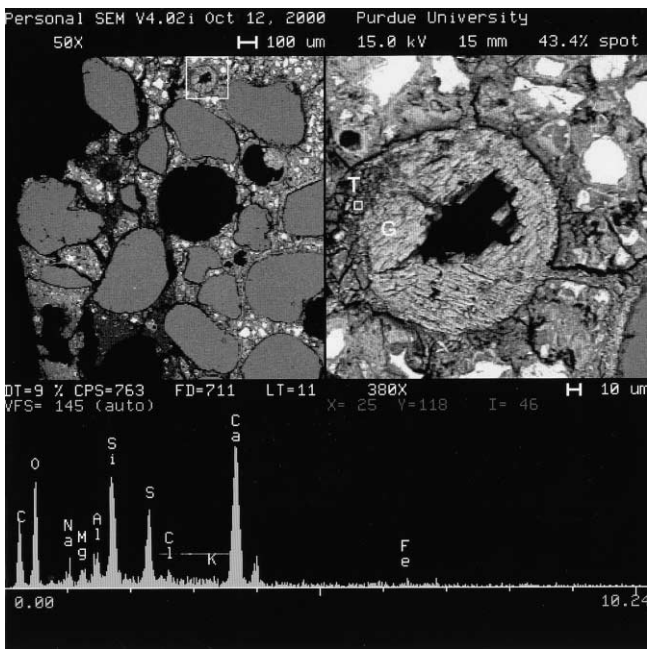

Fig. 8. SEM image of thaumasite (T) formation near a large deposit of gypsum (G).

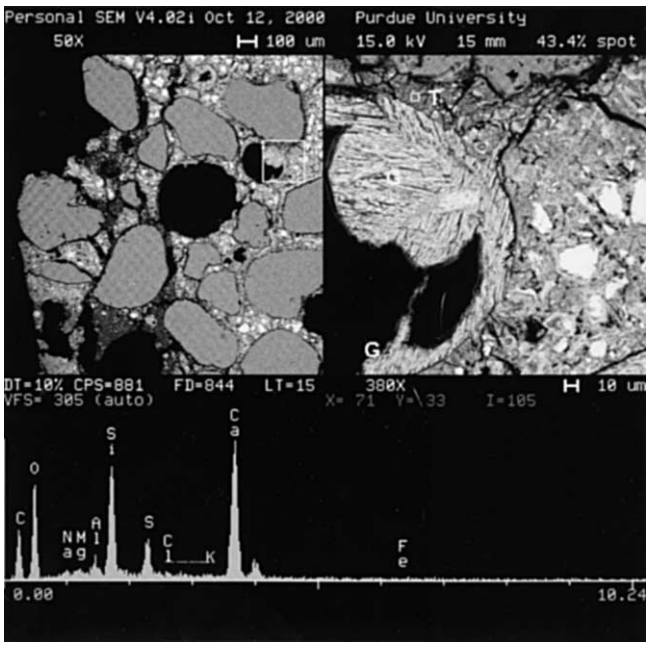

Fig. 9. SEM image of another region showing thaumasite (T) formation near a large gypsum (G) deposit.

sents thaumasite, while the other two spectra shown in Fig. 4(c and d) belong to ettringite and gypsum, respectively. Each of these single fiber spectra was the result of 200 s integration with a laser power of 1 mW per fiber. The result is a chemical image depicting the distribution of thaumasite, ettringite, and gypsum in the mixture. The light, dark, and grey regions correspond to gypsum, thaumasite, and ettringite, respectively.

Fig. 5(a) illustrates the chemical image from sulfate-attacked cement mortar surface. The image is composed of 6×6 (36) frames corresponding to a 420×336-μm^2 area of the surface. The total exposure time was 4 h (400 s/frame) using the $\times 20$ objective that corresponds to a 7×7-μm^2 area. Using the SAM classification algorithm after the data were preprocessed using SGSD, each pixel of the 2880 (60×48) pixels in the entire Raman image is categorized as thaumasite (dark), gypsum (light), or background (grey) based on the Raman spectrum associated with that pixel as shown in Fig. 5(b–d), respectively. Each of these single fiber spectra was the result of 400 s integration with a laser power of approximately 1 mW per fiber.

The SEM observations for the cement mortar specimen stored in sodium sulfate solution at 5°C are presented in Figs. 6, 7, 8, and 9. Thaumasite formation is evident in the regions close to the surface as confirmed by energy dispersive X-ray spot analyses (presented below the micrographs). The low magnification images in Figs. 6, 7, 8, and 9 show cracked regions near the surface full of dark deposits of thaumasite. In certain areas, as shown in Figs. 6 and 7, a large scale of conversion of C-S-H to thaumasite has occurred. Figs. 8 and 9 illustrate the formation of thaumasite close to the abundant deposits of gypsum near the surface.

4. Conclusion

Thaumasite formed in sulfate-attacked cement mortars is difficult to distinguish from ettringite by conventional XRD and SEM techniques because of their similar X-ray patterns and morphology. In this study, the distribution of thaumasite on the cement mortar surface was chemically mapped using NIRIM. Chemical imaging was able to differentiate thaumasite from gypsum and ettringite. The formation of thaumasite in these sulfate-attacked mortars was supported by SEM and energy dispersive X-ray analysis. Thus, NIRIM is a powerful tool that can be used to identify thaumasite and to differentiate it from ettringite and gypsum. This technique has the capability to play a major role in assessing the type and extent of sulfate attack.

Acknowledgments

This work was supported by the Office of Naval Research (N00014-99-0155).

References

[1] M.D. Cohen, A. Bentur, Durability of portland cement — Silica fume pastes in magnesium sulfate and sodium sulfate solutions, ACI Mater. J. 85-M3 (1988) 148–157.
[2] J. Bensted, Thaumasite — Background and nature in deterioration of cements, mortars, and concretes, Cem. Concr. Compos. 21 (1999) 117–121.
[3] M. Collepardi, Thaumasite formation and detrioration in historic buildings, Cem. Concr. Compos. 21 (1999) 147–154.
[4] S. Diamond, R.J. Lee, Microstructural alterations associated with sulfate attack in permeable concretes, in: J. Skalny, J. Marchand (Eds.), Material Science of Concrete — Sulfate Attack Mechanisms, American Ceramic Society, Westerville, OH, 1999, pp. 123–174.
[5] N.J. Crammond, M.A. Halliwell, The thaumasite form of sulfate attack in concretes containing a source of carbonate ions — A microstructural review, advances in concrete technology, Proceedings: Second CANMET/ACT International Symposium, Las Vegas, NV, USA, International Cement Microscopy Association, Duncanville, TX, (1995) 357–380.
[6] C. Rogers, M. Thomas, H. Lohse, Thaumasite from Manitoba and Ontario, 19th International Conference on Cement Microscopy, Cincinnati, USA, American Concrete Institute, Washington, D.C., 1997 pp. 306–319.
[7] R. Yang, N.R. Buenfeld, Microstructural identification of thaumasite in concrete by backscattered electron imaging at low vacuum, Cem. Concr. Res. 30 (2000) 775–779.
[8] R.A. Edge, H.F.W. Taylor, Crystal structure of thaumasite, Acta Crystallogr., Sect. B 27 (1971) 594–601.
[9] S.A. Hartshorn, J.H. Sharp, R.N. Swamy, Thuamasite formation in portland–limestone cement pastes, Cem. Concr. Res. 29 (1999) 1331–1340.
[10] C.L. Lobo, A Study on Type K Expansive Cement Paste and Concrete and the Influence of Silica Fume, PhD Thesis, Purdue University, 1991.
[11] A.D. Gift, J. Ma, K.S. Haber, B.L. McClain, D. Ben-Amotz, Near-infrared Raman imaging microscope based on fiber-bundle image compression, J. Raman Spectrosc. 30 (1999) 757–765.

[12] J. Ma, D. Ben-Amotz, Rapid micro-Raman imaging using fiber-bundle image compression, Appl. Spectrosc. 51 (1997) 1845–1848.
[13] B.L. McClain, J. Ma, D. Ben-Amotz, Optical absorption and fluorescence spectral imaging using fiber-bundle image compression, Appl. Spectrosc. 53 (1999) 1118–1122.
[14] B.L. McClain, H.G. Hedderich, A.D. Gift, D. Zhang, K.N. Jallad, K.S. Ma, J. Ma, D. Ben-Amotz, Fast chemical imaging. A rapid tool for medical, materials, and process analysis, Spectroscopy 15 (9) (2000) 28–37.
[15] L. Biel, D. Langrebe, Multispec — A Tool for Multispectral Image Data Analysis, 1996 (Pecora 13, Sioux Falls, SD).
[16] A. Savitsky, M.J.E. Golay, Smoothiing and differentiation of data by simplified least square procedures, Anal. Chem. 36 (1964) 1627–1639.
[17] D. Zhang, D. Ben-Amotz, Enhanced chemical classification of Raman images in the presence of strong fluorescence interference, Appl. Spectrosc. 54 (9) (2000) 1379–1383.
[18] S.P. Varma, J. Bensted, Studies of thaumasite, Silic. Ind. 38 (2) (1973) 29–32.
[19] J. Bensted, S.P. Varma, Studies of thaumasite — Part II, Silic. Ind. 29 (1) (1974) 11–19.